Detection of Flow-Regime Transitions Using Dynamic Mode Decomposition and Moving Horizon Estimation

Angelo Alessandri, Patrizia Bagnerini, Mauro Gaggero, Davide Lengani, and Daniele Simoni

***Abstract*— The spatial and time behaviors of fluid flows at different Reynolds numbers and free-stream turbulence intensity levels are studied by combining dynamic mode decomposition (DMD) and moving horizon estimation to detect flow-regime transitions. In more detail, the norm of residuals provided by DMD when processing successive snapshots of the flow velocity field shows a trend that is identified by means of a moving horizon estimator based on a switching model. This allows detecting the change from stable to unstable flow regimes, which in turn enables to extract modes, frequencies, and growth rates of complex structures such as vortices, characterizing the fluid flow in the spatial and temporal domains. Different cases of experimental measurements given by a particle image velocimetry are analyzed to recognize the complexity of the underlying flow physics, while showing the effectiveness of the proposed approach.**

***Index Terms*— Dynamic mode decomposition (DMD), fluid flow, moving horizon estimation (MHE), nonlinear switching systems.**

I. Introduction

THE transition process of boundary layers is a complex phenomenon that is widely studied in fluid dynamics. It depends on the Reynolds number (Re) and the free-stream turbulence intensity (FSTI) level [1]–[6]. Due to the need of dealing with a large amount of information on the fluid flow, the automatic detection of the dominant dynamics is usually difficult. Thus, low-order models are often employed to reduce the computational burden. These models enable to easily represent complex structures characterizing the flow, such as vortices in the spatial and temporal domains [7]–[9]. Toward this end, dynamic mode decomposition (DMD) has become quite a popular tool to construct reduced-order models that are useful to analyze fluid flows [10]. In more detail, the DMD procedure isolates the main dynamics of a flow and provides a synthetic representation of the dominant structures (the modes of decomposition) and their spatial and temporal evolutions. The computation of the modes, their frequencies, and their growth (or decay) rates allows identifying unstable waves that are responsible for transition from a stable to an unstable flow regime.

In this study, the best fitting in the least-squares sense of successive ensembles of velocity field snapshots is first determined by using DMD. Then, moving horizon estimation (MHE) is applied to the resulting DMD residuals to quickly and robustly identify changes of the regime. More specifically, two spatial regions are determined, which correspond to the stable and unstable flow regimes, respectively. This enables extracting the modes, frequencies, and growth/decay rates of the fluid flow in an accurate way by applying again DMD separately in the various regions instead of processing the entire data set at hand, which may lead to poor results. Finally, the growth/decay rates and frequencies computed by the proposed DMD/MHE technique are compared with those obtained experimentally, thus showing the effectiveness of the proposed approach.

In general, DMD provides a local linear approximation of complex spatio-temporal dynamics, which in principle may be used for the purpose of real-time control [11], [12]. Among the various DMD algorithms reported in the literature to construct reduced-order models, the method proposed in [10] allows projecting the sparse matrices of flow fields on a subspace of lower dimension. In [13], a different technique is proposed that is based on an orthonormal subspace representation and optimization with the conjugate gradient method. Another approach based on the subtraction from the whole data set of a sort of "mean snapshot" is presented in [14]. The DMD algorithm discussed in [15] consists in minimizing the effects of the noise by using an augmented snapshot matrix to be projected onto a subspace, irrespective of the method adopted for the computation of the modes. Low-order reduction is addressed also in [16] by solving a regularized least-squares problem to impose sparsity with the choice of a suitable penalization weight.

Modeling based on hybrid systems is nowadays well established in a number of applications [17], as it enables to account for the plant behavior over a large range of operating conditions [18]–[21]. Piecewise linear models are proposed in [22] to detect fluid flow transitions, and such models are identified and validated by using DMD. Instead, in this work, we explicitly deal with the switching from stability to instability regimes, whereas in [22] this aspect is faced only heuristically. Preliminary results on the application of MHE for the evaluation of DMD residuals to identify changes of the regime are reported in [23]. Based on the aforesaid, here the trend in the norm of DMD residuals is estimated to identify the switching between different regimes in boundary

Manuscript received August 7, 2019; revised October 29, 2019; accepted November 19, 2019. Date of publication April 20, 2020; date of current version April 12, 2021. Manuscript received in final form November 22, 2019. This work was supported in part by the AFOSR under Grant FA9550-15-1-0530. Recommended by Associate Editor C. Prieur. *(Corresponding author: Angelo Alessandri.)*

A. Alessandri, P. Bagnerini, D. Lengani, and D. Simoni are with the University of Genoa (DIME), 16145 Genoa, Italy (e-mail: alessandri@dime.unige.it; bagnerini@dime.unige.it; davide.lengani@edu.unige.it; daniele.simoni@unige.it).

M. Gaggero is with the National Research Council of Italy (INM), 16149 Genoa, Italy (e-mail: mauro.gaggero@cnr.it).

Color versions of one or more of the figures in this article are available online at https://ieeexplore.ieee.org.

Digital Object Identifier 10.1109/TCST.2019.2956027

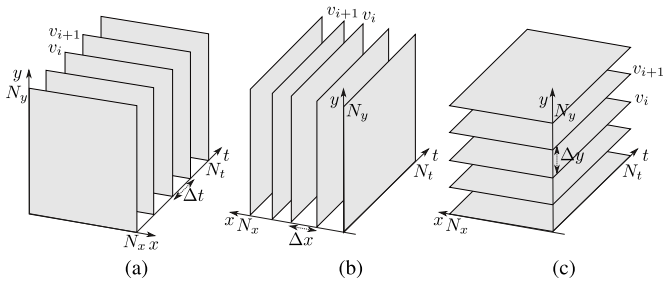

Fig. 1. (a) Sketch of the snapshots following a temporal evolution, (b) a spatial evolution along the x-direction, and (c) a spatial evolution along the y-direction, i.e., with $n_v = N_x N_y$, $n_v = N_t N_y$, and $n_v = N_t N_x$, respectively.

layers. Specifically, we focus on the change from a stable (usually referred to as pre-transitional) regime to an unstable (also named transitional) one [24]–[27]. Toward this end, the identification of a trend is cast as a constrained state estimation problem subject to switching [28], [29]. The proposed method is applied to an experimental data set obtained by a time-resolved particle image velocimetry (TR-PIV) to study the transition processes of boundary layers growing with a strong adverse pressure gradient.

In the last decades, a lot of attention has been devoted to the estimation of systems in which continuous and discrete states (DSs) interact dynamically. Among the various alternatives reported in the literature, we focus on MHE, as this approach is characterized by an intrinsic robustness to noises and is well suited to performing estimation in the presence of constraints [30], [31]. Recent investigations on MHE have concerned the reduction of the computational burden [32], [33], which is fundamental for real-time applications. In the context of fluid flows, we show that MHE is able to identify the different flow regimes associated with the occurrence of a switching.

The rest of this work is organized as follows. The DMD algorithm is presented in Section II. The proposed method for residual trend identification based on MHE is described in Section III. The results on the application of such an approach on experimental data sets are showcased in Section IV. Finally, conclusions are given in Section V.

Throughout the manuscript, we adopt the following notation. The symbol (x, y), where x and y are column vectors, stands for $[x^\top, y^\top]^\top$. Given a real vector v, $|v| := (v^\top v)^{1/2}$ denotes its Euclidean norm. The Frobenius norm of a real matrix M is given by $|M|_F := (\mathrm{tr}(M^\top M))^{1/2}$. Given a complex matrix C, C^* denotes its Hermitian. A function $\varphi : [0, +\infty) \to \mathbb{R}$ is said to be a K-function if it is continuous, strictly monotone increasing, and such that $\varphi(0) = 0$.

II. Dynamic Mode Decomposition

We consider the DMD approach presented in [10], which allows finding a linear model that approximates the underlying flow dynamics and can also provide additional information. Toward this end, let us denote by $v_i \in \mathbb{R}^{n_v}$ the snapshot of a two-dimensional velocity field according to a temporal or spatial evolution, as shown, for instance, in Fig. 1(a), where the vectors v_i are associated with N_x measuring points in the streamwise direction and N_y measuring points in the wall-normal direction over N_t time instants. Let $V_1^k := \mathrm{col}(v_1, v_2, \ldots, v_k)$ and $V_2^{k+1} := \mathrm{col}(v_2, \ldots, v_{k+1})$ be the matrices resulting from the collection of the snapshots from 1 to k and from 2 to $k+1$, respectively. We assume that, given the sequence $v_1, \ldots, v_k, v_{k+1} \in \mathbb{R}^{n_v}$, the dynamics is described by a linear mapping $A \in \mathbb{R}^{n_v \times n_v}$, i.e., $v_{k+1} = A v_k$. Thus, we can write

$$V_1^k = \mathrm{col}(v_1, Av_1, \ldots, A^{k-1} v_1)\,.$$

The purpose of the DMD procedure is to extract the flow information of the physical phenomenon described by A without the need of finding A, which may be of large dimension. Thus, if the column vectors of V_1^k become linearly dependent as the number of snapshots increases, the dimensionality issues are reduced by letting v_{k+1} be a linear combination of $v_1, v_2, \ldots, v_k$, that is

$$v_{k+1} = a_1 v_1 + a_2 v_2 + \cdots + a_k v_k + \rho = V_1^k a + \rho$$

where $a := (a_1, \ldots, a_k) \in \mathbb{R}^k$ and $\rho \in \mathbb{R}^{n_v}$ is a residual to be minimized according to [10]. If we define $e_k := (0, \ldots, 0, 1) \in \mathbb{R}^k$, we obtain

$$V_2^{k+1} = \mathrm{col}(v_2, \ldots, V_1^k\, a) + \rho\, e_k.$$

The previous expression is equivalent to

$$V_2^{k+1} = V_1^k\, S + \rho\, e_k$$

where S is a companion matrix given by

$$S := \begin{pmatrix} 0 & 0 & \cdots & \cdots & a_1 \\ 1 & 0 & \cdots & \cdots & a_2 \\ 0 & \ddots & \ddots & & \vdots \\ \vdots & \ddots & 1 & 0 & a_{k-1} \\ 0 & \cdots & 0 & 1 & a_k \end{pmatrix} \in \mathbb{R}^{k \times k}.$$

To sum up, DMD consists in finding the solution of the optimization problem

$$\min_{S \in \mathcal{S}} \left| V_2^{k+1} - V_1^k\, S \right|_F^2 \tag{1}$$

where $\mathcal{S}$ denotes the set of all real matrices having the companion structure above. Then, flow information is extracted from the projection $\tilde{S}_k^\circ \in \mathbb{R}^{k \times k}$ of the optimal matrix $S_k^\circ := \arg\min_{S \in \mathcal{S}} |V_2^{k+1} - V_1^k\, S|_F^2$ on the proper orthogonal decomposition modes. In more detail, the overall DMD procedure is composed of the steps reported in Algorithm 1, which, for all k, provides the matrix $\tilde{S}_k^\circ$ as final outcome. In Algorithm 1, Δp is the step between snapshots, which may be equal to Δt, Δx, or Δy (see Fig. 1).

Complex structures such as vortices in the flow can be localized by analyzing the matrix $\tilde{S}_k^\circ$. In general, it is more convenient to use $\tilde{S}_k^\circ$ instead of S_k° since the extraction of flow information from S_k° is ill-conditioned, with the consequence that only the largest modes can be precisely identified [10]. The real part of the eigenvalues of $\tilde{S}_k^\circ$ provides the growth/decay rate of the structure identified by the corresponding DMD mode, whereas the imaginary part provides the

Algorithm 1 Steps of the DMD Algorithm

Inputs: V_1^k, V_2^{k+1}.
Main steps:

1: Compute the singular value decomposition of V_1^k, i.e., two unitary matrices U and W and a diagonal matrix Σ such that $V_1^k = U\Sigma W^*$, where W^* is the complex conjugate of W.
2: Compute the projection of the matrix S_k° on the proper orthogonal decomposition modes, i.e., $\tilde{S}_k^\circ := U^* V_2^{k+1} W \Sigma^{-1}$.
3: Compute the matrices of eigenvectors and eigenvalues of the matrix $\tilde{S}_k^\circ$, i.e., Y and D (diagonal).
4: Compute the matrix of the DMD modes $\Theta_k := UY$.
5: Compute the diagonal matrix P_k of the logarithms of the DMD eigenvalues of $\tilde{S}_k^\circ$, i.e., $P_k := \log(D)/(2\pi\Delta p)$.

Outputs: $\tilde{S}_k^\circ$, Θ_k, P_k.

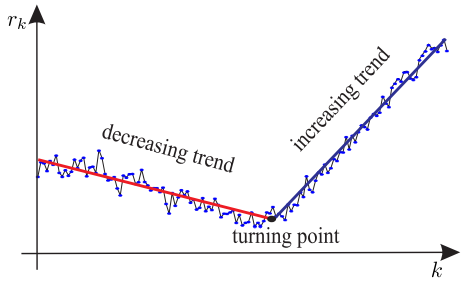

Fig. 2. Two different trends of residuals resulting from the application of the DMD procedure.

frequency of the vortex shedding. Positive growth rates indicate growing structures, leading to the generation of unstable waves within the flow. The unstable regime of the boundary layer is then identified as the region where positive growth rates are measured. On the contrary, the stable regime is characterized by negative or null growth rates.

The aim of this study is to identify the position of the switching between the pre-transitional (stable) region and the transitional (unstable) one. This enables applying the DMD procedure separately in the various regions in order to compute in an accurate way frequencies and growth rates of the structures characterizing the flow. Toward this end, in order to identify the switching, we sequentially apply the DMD algorithm over a region of increasing size and with a larger amount of snapshots. This corresponds to an increase in the dimension of the data matrices V_1^k and V_2^{k+1}. The variation of the slope in the trend of the residuals identifies the turning point of the switching between the stable region and the unstable one (see Fig. 2 for an example of switching of a residual trend). The reason of this trend behavior lies in the fact that the pre-transitional regime is ruled by linear effects and low velocity fluctuations, and therefore the DMD residuals decrease when the number of snapshots increases. Instead, the velocity fluctuations in the transitional regime increase significantly, and hence also the DMD residuals grow.

In more detail, after choosing a sufficiently large k_0 (a certain number of column vectors in V_1^k is necessary to apply the DMD algorithm in a reliable way), we sequentially process the snapshots from 1 to k using DMD, with k varying from k_0 to N_p, where N_p corresponds to N_t, N_x, or N_y depending on whether a temporal or spatial analysis is performed, according to Fig. 1 (in this work, we have focused on a spatial analysis). In other words, we apply DMD to the matrices V_1^k and V_2^{k+1} chosen with k varying as described above. Let $R_k := V_2^{k+1} - V_1^k \tilde{S}_k^\circ$ be the corresponding residual matrix with k columns. In order to identify the change of regime, we employ the cumulative average r_k of the Euclidean norm of the columns of R_k, that is

$$r_k := \frac{\sum_{j=1}^{k} |R_k^j|}{k} \tag{2}$$

for increasing values of k, where R_k^j is the jth column of R_k. In Section III, we propose to use MHE to detect a change in the trend of the cumulative average r_k.

III. Estimation of Trend Dynamics

To detect changes of the regime in the fluid flow, we rely on a simple switching dynamics with state $\xi_k := (\xi_{1,k}, \xi_{2,k})$ for modeling the trend of DMD residuals with turning point as in Fig. 2. More specifically, we consider a switching nonlinear second-order system with two DSs, as follows:

$$\text{DS\#1} \quad \begin{cases} \xi_{1,k+1} = \xi_{2,k}\, \xi_{1,k} \\ \xi_{2,k+1} = a_1 \\ z_k = \xi_{1,k} \end{cases} \tag{3a}$$

$$\text{DS\#2} \quad \begin{cases} \xi_{1,k+1} = \xi_{2,k}\, \xi_{1,k} \\ \xi_{2,k+1} = a_2 \\ z_k = \xi_{1,k} \end{cases} \tag{3b}$$

where $k = 0, 1, \ldots$ with $a_1 \in (0, 1)$ and $a_2 > 1$ unknown. DS#1 accounts for a decreasing trend, while DS#2 refers to an increasing one, with rates a_1 and a_2, respectively. The variable z_k represents the output of the system, and measurements of it are available. Note that a switching first-order model would be sufficient if we knew a_1 and a_2 exactly.

The problem of identifying the trend reduces to find the constrained estimates of the unknowns a_1 and a_2 together with a decision on the turning point, which is unknown. Since such estimates may be affected by disturbances, we propose to use an estimation approach based on MHE, which appears to be well suited to performing this task owing to its intrinsic robustness. Toward this end, first of all we consider the more general problem to estimate the state of a switching discrete-time system by using MHE. Later, we will turn back to (3).

Consider the general dynamic system

$$\xi_{k+1} = f_{\lambda_k}(\xi_k) + w_k \tag{4a}$$

$$z_k = h_{\lambda_k}(\xi_k) + v_k \tag{4b}$$

where $k = 0, 1, \ldots$, $\xi_k \in \mathbb{R}^n$ is the continuous state, $\lambda_k \in \Lambda := \{1, \ldots, q\}$ is the DS, $w_k \in W \subset \mathbb{R}^n$ is the system disturbance, $v_k \in V \subset \mathbb{R}^m$ is the measurement disturbance, and $z_k \in \mathbb{R}^m$ is the output. The functions $f_i : \mathbb{R}^n \to \mathbb{R}^n$ and $h_i : \mathbb{R}^n \to \mathbb{R}^m$, $i = 1, \ldots, q$, are smooth. The sets W and V are assumed to be compact. System (4) may be subject to equality or inequality constraints, that is

$$l_{\lambda_k}(\xi_k) = 0 \tag{5a}$$

$$g_{\lambda_k}(\xi_k) \leq 0 \tag{5b}$$

for $k = 0, 1, \ldots$, where the functions $l_i : \mathbb{R}^n \to \mathbb{R}^{n_l}$ and $g_i : \mathbb{R}^n \to \mathbb{R}^{n_g}$, $i = 1, \ldots, q$, are smooth. Since the goal consists in devising a moving horizon estimator, we rely on the most recent batch of output measurements, which we collect in the vector $z_{k-N}^k := (z_k, z_{k-1}, \ldots, z_{k-N})$. Concerning the DSs, not all the possible combinations of them may occur in general. Therefore, after defining by $\lambda_{k-N}^k := (\lambda_k, \lambda_{k-1}, \ldots, \lambda_{k-N})$ a generic switching pattern from $k-N$ to k, let us denote by Λ_0^N the set of admissible patterns and by $\Lambda_\alpha^{N-\omega}$ its restriction from α to $N-\omega$ for some integers $\alpha \geq 0$ and $\omega \geq 0$ such that $\alpha + \omega \leq N$. Moreover, let

$$H_N\left(\xi_{k-N}, \lambda_{k-N}^k\right) := \begin{pmatrix} h_{\lambda_k} \circ f_{\lambda_{k-1}} \circ f_{\lambda_{k-2}} \circ \cdots \circ f_{\lambda_{k-N}}(\xi_{k-N}) \\ h_{\lambda_{k-1}} \circ f_{\lambda_{k-2}} \circ \cdots \circ f_{\lambda_{k-N}}(\xi_{k-N}) \\ \vdots \\ h_{\lambda_{k-N+1}} \circ f_{\lambda_{k-N}}(\xi_{k-N}) \\ h_{\lambda_{k-N}}(\xi_{k-N}) \end{pmatrix} \in \mathbb{R}^{(N+1)m}.$$

Assumption 1: There exists $\Xi \subset \mathbb{R}^n$ compact such that, for all $w_k \in W$, $v_k \in V$, and admissible $\lambda_k \in \Lambda$, we have $\xi_k \in \Xi$ for all $k = 0, 1, \ldots$. □

As pointed out in [28] and [34], unless $m \geq n$, in general, it is not possible to detect switches that occur in the first or in the last stages of a moving observation batch. As a consequence, one can deal with a restricted batch, i.e., $z_{k-N+\alpha}^{k-\omega}$ instead of z_{k-N}^k, to uniquely determine the DS in the restricted interval from $k-N+\alpha$ to $k-\omega$.

We assume the following, which corresponds to the notion of observability presented in [34].

Assumption 2: There exist nonnegative α, ω together with the following:

1) a K-function $\psi_{\bar{\lambda}_0^N, \tilde{\lambda}_0^N}(\cdot)$ such that

$$\psi_{\bar{\lambda}_0^N, \tilde{\lambda}_0^N}(|(\bar{\xi}, \bar{\xi}') - (\tilde{\xi}, \tilde{\xi}')|^2) \leq \left|H_N(\bar{\xi}, \bar{\lambda}_0^N) - H_N(\bar{\xi}', \tilde{\lambda}_0^N) - \left(H_N(\tilde{\xi}, \bar{\lambda}_0^N) - H_N(\tilde{\xi}', \tilde{\lambda}_0^N)\right)\right|^2 \quad \forall \bar{\xi}, \bar{\xi}', \tilde{\xi}, \tilde{\xi}' \in \Xi \tag{6}$$

for every $\bar{\lambda}_0^N, \tilde{\lambda}_0^N \in \Lambda_0^N$ with $\bar{\lambda}_\alpha^{N-\omega} \neq \tilde{\lambda}_\alpha^{N-\omega}$;

2) a K-function $\varphi_{\lambda_0^N}(\cdot)$ such that

$$\varphi_{\lambda_0^N}(|\bar{\xi} - \tilde{\xi}|^2) \leq \left|H_N(\bar{\xi}, \lambda_\alpha^{N-\omega}) - H_N(\tilde{\xi}, \lambda_\alpha^{N-\omega})\right|^2 \quad \forall \bar{\xi}, \tilde{\xi} \in \Xi \tag{7}$$

for every $\lambda_0^N \in \Lambda_0^N$ and $\lambda_\alpha^{N-\omega} \in \Lambda_\alpha^{N-\omega}$.

□

The assumption above turns out to be quite simplified for (3). Toward this end, using the same notation adopted for (4), system (3) can be written as follows:

$$\xi_{k+1} = f_{\lambda_k}(\xi_k) \tag{8a}$$

$$z_k = \xi_{1,k} \tag{8b}$$

where

$$\xi_k := \left(\xi_{1,k},\ \xi_{2,k}\right), \quad f_{\lambda_k}(\xi_k) := \left(\xi_{1,k}\, \xi_{2,k},\ \xi_{2,k}\right)$$

with $\xi_{2,k} = a_i$ and $\lambda_k = i$, $i = 1, 2$. In the case of $N = 1$ (i.e., a moving window with only two measures), we deal with z_{k-1}^k, and hence, to simplify the notation, let us refer to

$$z_0^1 = H_1\left(\xi_0, \lambda_0^1\right) = \left(\xi_{1,0}\, \xi_{2,0},\ \xi_{1,0}\right).$$

The simultaneous distinguishability of the continuous state and DS of (8) corresponds to the satisfaction of the following:

$$H_1(\bar{\xi}_0, \bar{\lambda}_0^1) = H_1(\tilde{\xi}_0, \tilde{\lambda}_0^1) \Rightarrow \bar{\xi}_0 = \tilde{\xi}_0 \text{ and } \bar{\lambda}_0 = \tilde{\lambda}_0 \tag{9}$$

with $\bar{\xi}_0, \tilde{\xi}_0 \in \mathbb{R}^2$ and $\bar{\lambda}_0^1, \tilde{\lambda}_0^1 \in \Lambda_0^1$. Such a condition is trivially satisfied for non-null $\bar{\xi}_{1,0}, \tilde{\xi}_{1,0}$, which is necessary for the switching patterns $(\star, 1)$ and $(\star, 2)$ to be distinguishable, i.e., $\alpha = 0$ and $\omega = 1$.

In general, we need to assume that the functions describing the state equations are Lipschitz. In the case of (3), this is easily satisfied.

Assumption 3: The functions f_λ and h_λ are of class C^2 and Lipschitz, that is

$$|f_\lambda(\xi) - f_\lambda(\xi')| \leq c_f\, |\xi - \xi'| \quad \forall \xi, \xi' \in \Xi$$
$$|h_\lambda(\xi) - h_\lambda(\xi')| \leq c_h\, |\xi - \xi'| \quad \forall \xi, \xi' \in \Xi$$

for some $c_f, c_h > 0$ and independently of $\lambda \in \Lambda$. □

An MHE strategy for (4) provides a state estimate that minimizes the least-squares cost

$$\begin{aligned} J_k\left(\hat{\xi}_{k-N+\alpha}, \hat{\lambda}_{k-N+\alpha}^{k-\omega}\right) &= \mu\, |\hat{\xi}_{k-N+\alpha} - \bar{\xi}_{k-N+\alpha}|^2 + \sum_{i=k-N+\alpha}^{k-\omega} \left|z_i - h_{\hat{\lambda}_i}\left(\hat{\xi}_i\right)\right|^2 \\ &= \mu\, |\hat{\xi}_{k-N+\alpha} - \bar{\xi}_{k-N+\alpha}|^2 \\ &\quad + \left|z_{k-N+\alpha}^{k-\omega} - H_N\left(\hat{\xi}_{k-N+\alpha}, \hat{\lambda}_{k-N+\alpha}^{k-\omega}\right)\right|^2 \end{aligned} \tag{10}$$

where $\mu \geq 0$ and $\hat{\xi}_{k-N+\alpha}$ and $\hat{\lambda}_{k-N+\alpha}^{k-\omega}$ are the estimates of $\xi_{k-N+\alpha}$ and $\lambda_{k-N+\alpha}^{k-\omega}$, respectively. The quantity $\bar{\xi}_{k-N+\alpha}$ is a "prediction" of $\xi_{k-N+\alpha}$, whose choice will be described later.

Thus, we can state the following problem to be solved for all values of k.

Problem Optimal MHE (OMHE): Find a solution to

$$\min_{\hat{\xi}_{k-N+\alpha} \in \Xi, \hat{\lambda}_{k-N+\alpha}^{k-\omega} \in \Lambda_\alpha^{N-\omega}} J_k(\hat{\xi}_{k-N+\alpha}, \hat{\lambda}_{k-N+\alpha}^{k-\omega})$$
$$\text{s.t. } \hat{\xi}_{i+1} = f_{\hat{\lambda}_i}(\hat{\xi}_i) \quad i = k-N+\alpha, \ldots, k-\omega-1$$
$$l_{\hat{\lambda}_i}(\hat{\xi}_i) = 0, \quad i = k-N+\alpha, \ldots, k-\omega$$
$$g_{\hat{\lambda}_i}(\hat{\xi}_i) \leq 0, \quad i = k-N+\alpha, \ldots, k-\omega$$

at each k. □

After obtaining the optimal solutions $\hat{\xi}_{k-N+\alpha}^\circ$ and $\hat{\lambda}_{k-N+\alpha}^{k-\omega\ \circ}$ of Problem OMHE at step k, a convenient choice for the prediction of $\xi_{k-N+\alpha+1}$ is letting $\bar{\xi}_{k-N+\alpha+1} = f_{\hat{\lambda}_{k-N+\alpha}^\circ}(\hat{\xi}_{k-N+\alpha}^\circ)$. Based on this prediction, we solve again Problem OMHE at the next step $k+1$ and so on.

The solution of Problem OMHE provides an exponentially bounded estimation error $e_{k-N+\alpha} := \xi_{k-N+\alpha} - \hat{\xi}_{k-N+\alpha}^\circ$, i.e., there exist $a \in (0, 1)$ and $b > 0$ such that $|e_{k-N+\alpha}| \leq |e_0| a^k + b$, $k = N, N+1, \ldots$, where e_0 is the initial error.

Theorem 1: Under Assumptions 1–3, if

$$\delta := \min_{\lambda_0^N \in \Lambda_0^N} \left\{ \inf_{\xi,\xi' \in \Xi, \xi \neq \xi'} \frac{\varphi_{\lambda_0^N}(|\xi - \xi'|^2)}{|\xi - \xi'|^2} \right\} > 0 \tag{12}$$

and if $\mu \geq 0$ is such that

$$\frac{8\,\mu\,c_f^2}{\mu + \delta} < 1 \tag{13}$$

then the estimation error is exponentially bounded.

Proof: This theorem is equivalent to [34, Th. 4, p. 3281]. The proof is based on the use of lower and upper bounds on the cost (10) in line with previous results reported in the literature [35, Th. 1, p. 1758]. □

If system (4) is treated in a noise-free setting (i.e., both w_k and v_k are identically zero), then the estimation error is not asymptotically stable to zero in general (see [36]). Indeed, in the special case of (8), we can prove that the estimation error is asymptotically stable. Toward this end, first let us verify that (7) holds for (8). Since

$$\frac{\partial H_1\left(\xi_{k-N}, \lambda_{k-N}^{k-N+1}\right)}{\partial \xi_{k-N}} = \begin{pmatrix} \xi_{2,k-N} & \xi_{1,k-N} \\ 1 & 0 \end{pmatrix} \tag{14}$$

the rank of (14) is maximum and (9) is satisfied if $\xi_{1,k-N} \neq 0$. Therefore, we can apply [37, Proposition 8, p. 1036] and conclude that there exists $\delta_0 > 0$ such that

$$\sqrt{\delta_0}\left|\xi_{k-N} - \xi'_{k-N}\right| \leq \left|H_1\left(\xi_{k-N}, \lambda_{k-N}^{k-N+1}\right) - H_1\left(\xi'_{k-N}, \lambda'^{k-N+1}_{k-N}\right)\right| \tag{15}$$

holds over any compact subset Ξ_0 of the open positive orthant of $\mathbb{R}^2$. Moreover, let us denote by c_0 the Lipschitz constant of (8a) over Ξ_0.

Theorem 2: If we choose $\mu \in [0, \delta_0/c_0^2)$, then the estimation error given by the solution of Problem OMHE for system (8) over Ξ_0 is exponentially stable to zero.

Proof: Since

$$\left|H_1\left(\xi_{k-N}, \lambda_{k-N}^{k-N+1}\right) - H_1\left(\hat{\xi}_{k-N}, \hat{\lambda}_{k-N}^{k-N+1}\right)\right| \leq \left|H_N\left(\xi_{k-N}, \lambda_{k-N}^{k}\right) - H_N\left(\hat{\xi}_{k-N}, \hat{\lambda}_{k-N}^{k}\right)\right|$$

for $N > 1$, from (15) it follows that

$$\delta_0\left|\xi_{k-N} - \hat{\xi}_{k-N}\right|^2 \leq \left|H_N\left(\xi_{k-N}, \lambda_{k-N}^{k}\right) - H_N\left(\hat{\xi}_{k-N}, \hat{\lambda}_{k-N}^{k}\right)\right|^2 \tag{16}$$

holds for all $\xi_{k-N}, \hat{\xi}_{k-N} \in \Xi_0$ and $N > 1$. Using (16), we obtain a lower bound on the optimal cost, as follows:

$$\delta_0\left|\xi_{k-N} - \hat{\xi}^\circ_{k-N}\right|^2 \leq J_k\left(\hat{\xi}^\circ_{k-N}, \hat{\lambda}^{k\,\circ}_{k-N}\right) \tag{17}$$

and, by the definition of point of optimum, the following upper bound holds as well:

$$\begin{aligned} J_k\left(\hat{\xi}^\circ_{k-N}, \hat{\lambda}^{k\,\circ}_{k-N}\right) &\leq J_k\left(\xi_{k-N}, \lambda_{k-N}^{k}\right) \\ &= \mu\left|\xi_{k-N} - \bar{\xi}_{k-N}\right|^2 \\ &= \mu\left|f_{\lambda_{k-N-1}}(\xi_{k-N-1}) - f_{\hat{\lambda}^\circ_{k-N-1}}\left(\hat{\xi}^\circ_{k-N-1}\right)\right|^2. \end{aligned}$$

Owing to the distinguishability of the DS at the beginning of the moving window (i.e., $\hat{\lambda}^\circ_{k-N-1}$ is correctly estimated with λ_{k-N-1}) and the Lipschitz assumption, we get

$$J_k\left(\hat{\xi}^\circ_{k-N}, \hat{\lambda}^{k\,\circ}_{k-N}\right) \leq \mu\, c_0^2\left|\xi_{k-N-1} - \hat{\xi}^\circ_{k-N-1}\right|^2. \tag{18}$$

Using (17) and (18), it follows that:

$$\delta_0\left|e_{k-N}\right|^2 \leq \mu\, c_0^2\left|e_{k-N-1}\right|^2.$$

Therefore, it easy to conclude about the exponential stability of the estimation error. □

Theorems 1 and 2 enable to perform trend estimation based on MHE with stability guarantees. In Section IV, the results obtained by combining DMD and MHE in a real case study are detailed and discussed.

IV. Experimental Results

In this section, we present the results obtained with a large data set of velocity measurements, collected on a plate of chord of length $c = 200$ mm installed between two contoured walls inducing boundary layer separation. A TR-PIV has been used to measure both the streamwise and wall-normal velocity components. A collection of eight data sets corresponding to three different Reynolds numbers (based on the plate length and inlet velocity) and three different FSTI levels (defined at the plate leading edge) in the ranges $[40\,000, 90\,000]$ and $[0.65\%, 2.87\%]$, respectively, have been analyzed. For each data set, two time sequences of 3100 instantaneous snapshots have been acquired at 3168 Hz, which is at least ten times the vortex shedding frequency measured in the worst condition, i.e., high Re cases. To provide a statistically representative distribution of results, the acquisition time has been chosen sufficiently long to be split in several temporal intervals of length N_t, selected so as to represent about ten cycles of the vortical structures driving the transition. For the low Re and FSTI cases, ten time intervals have been analyzed (collected in three data sets), while for high Re and FSTI, we have considered 35 time intervals (grouped into six data sets). Overall, we have applied 240 times the MHE procedure described in Section III with different Re and FSTI conditions.

First, the MHE approach has been adopted to estimate the change of regime in the fluid flow, i.e., from the stable regime to the unstable one. Therefore, we have taken sequences of repeated "1" followed by repeated "2" as admissible switching patterns, as $\Lambda = \{1, 2\}$. Then, the modes, frequencies, and growth/decay rates of the flow have been computed in the identified regions (stable and unstable) separately. This provides much better results than those obtained by applying DMD to the entire data set at hand.

The MHE trend estimator described in (8) has been applied to the residuals r_k defined in (2) as output variables z_k. Referring to Fig. 1, the snapshot matrices V_1^k and $V_2^{k+1} \in \mathbb{R}^{n_v}$ have been considered in the spatial evolution, i.e., we have $n_v = N_t\, N_y$. DMD has been sequentially applied by increasing the number of snapshots from the first measuring point up to span the whole measurement domain in the streamwise direction, i.e., from $k = k_0$ to $k = N_x$, where $k_0 = 20$ and $N_x = 130$. The MHE algorithm has been initialized with

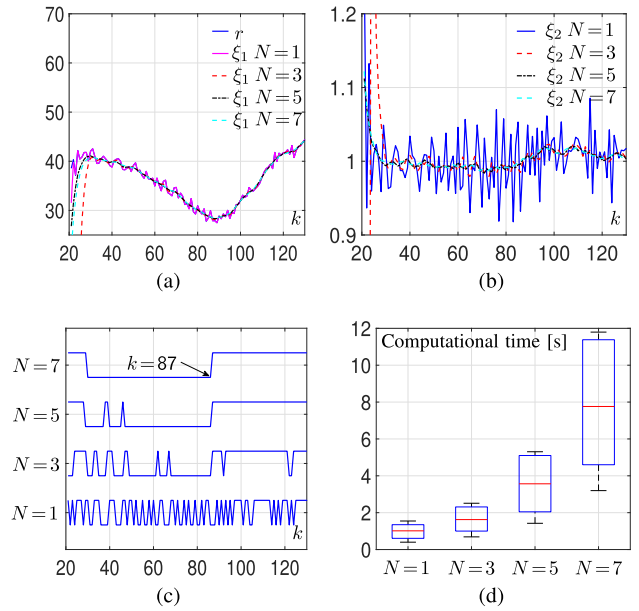

Fig. 3. (a) DMD residuals and corresponding estimates, (b) estimates of the second state variable, (c) estimated DSs, and (d) boxplots of the computational times obtained by MHE with different values of the horizon N.

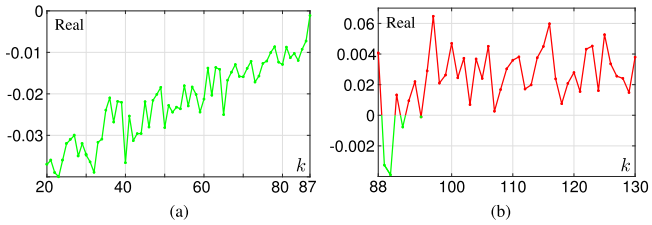

Fig. 4. Example of growth rates obtained by the DMD procedure with k varying in the (a) stable regime for $k = 20, \ldots, 87$ and in the (b) unstable one for $k = 88, \ldots, 130$. The growth rates are depicted in green if negative (stable) and in red if positive (unstable).

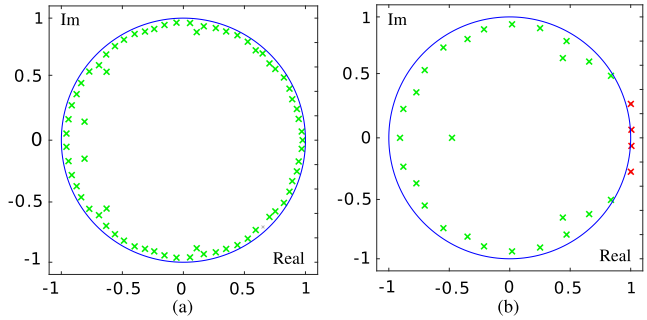

Fig. 5. Poles resulting from DMD in the (a) stable regime and in the (b) unstable one (stable eigenvalues are in green, while unstable ones are in red).

a prediction of the first state randomly generated by using a Gaussian distribution with mean equal to the real state and covariance equal to the identity matrix.

We have solved various Problems OMHE on a computer equipped with a 2.5-GHz Intel Xeon CPU and 16 GB of RAM by using the *fmincon* MATLAB routine with constraints given by the positivity of the variables and the kind of the trend. The results shown in Figs. 3–5 refer to the case study with Re $= 75\,000$ and FSTI $= 0.65\%$ for the first time range (of length $N_t = 310$).

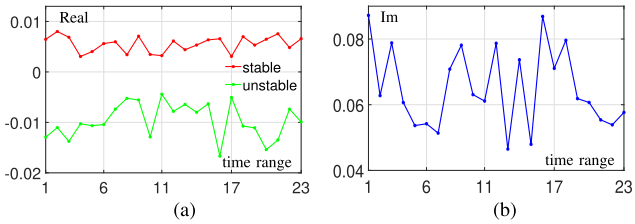

Fig. 6. (a) Growth rates of each time range in the stable regime (green) and in the unstable one (red) and (b) corresponding frequencies in the unstable regime.

The results of the application of the MHE approach with $\mu = 10$ are summarized in Fig. 3. A turning point between the stable and the unstable regime at $k = 87$ is identified by the MHE trend estimator with horizon $N = 7$ [see Fig. 3(c), where DS#1 and DS#2 are represented by the low and high values of the step, respectively]. Thus, it turns out that the MHE approach with a suitable choice of μ and N is able to identify the decreasing/increasing trend of residuals. More specifically, μ is required to be large enough to make the trend estimate robust to noises. For the same reason, we need to select a sufficiently large horizon N. This is particularly evident for the estimate of $\xi_{2,k}$, which is very noisy for small N [see Fig. 3(b)]. The estimation accuracy of the state variable $\xi_{1,k}$ is less sensitive to the choices of μ and N [see Fig. 3(a)]. Concerning the computational effort, reported in Fig. 3(d), the higher the horizon N, the larger the computational times, as the solution of Problem OMHE is more computationally demanding if N increases. It is worth noting that the use of classical approaches to estimation such as those based on Kalman filtering is not straightforward, as the trend model strongly relies on both switching and state constraints.

Fig. 4 reports the growth rates for different values of k and confirms that the identification of the switching between the regimes at $k = 87$ obtained by the MHE algorithm is correct. In more detail, in Fig. 4(a) the value of k varies in the stable regime (corresponding to the values up to $k = 87$), whereas in Fig. 4(b) it varies in the unstable regime from $k = 88$ to $k = 130$. The results make it clear that the larger are the number of snapshots in the case of the first regime (i.e., the larger is k), the higher are the growth rates, even if they remain stable (i.e., negative). Conversely, the second flow regime exhibits unstable (i.e., positive) eigenvalues for almost all the values of k.

Fig. 5 depicts the layout of the poles, i.e., the eigenvalues of the matrix $\tilde{S}_k^\circ$, as computed at step 3 of Algorithm 1, in the stable and unstable flow regimes. In the pre-transitional part of the boundary layer, as shown in Fig. 5(a), only stable eigenvalues are present. On the contrary, in the transitional regime [see Fig. 5(b)], four unstable poles causing the boundary layer transition to the unstable regime appear.

As said, the proposed procedure based on the combination of DMD and MHE has been applied many times for different time ranges. Fig. 6(a) illustrates the growth rates of each time range in the stable flow regime, while Fig. 6(b) shows the growth rates associated with the unstable one. The results indicate that the first flow regime is essentially stable, as no unstable eigenvalues have been observed for all the time instants. Conversely, the second regime shows a variable

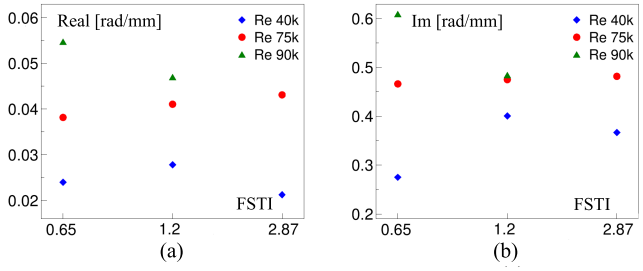

Fig. 7. (a) Time-mean growth rate and (b) time-mean frequency.

number of unstable eigenvalues at various time instants, with different growth rates and frequencies.

To verify whether the results obtained by the proposed approach correctly identify the properties of the flow in the unstable regime where vortices are generated, the growth rates and frequencies computed by the proposed DMD/MHE technique have been compared with those obtained in the reference literature. Toward this end, Fig. 7(a) shows the time-mean values of the maximum growth rate, while Fig. 7(b) reports the time-mean frequency. Such values confirm the expected results with different values of Re and FSTI. In particular, the Reynolds number has the largest impact on the mean growth rate, while the variation of the FSTI has a lower effect on the growth rate, as discussed also in [25]. A similar effect may be observed on the mean frequency, as expected [38].

The plots in Fig. 8 showcase the real and imaginary parts of the DMD mode Θ_v of the wall-normal velocity component v, which are useful to illustrate the velocity fluctuations in the wall-normal coordinate and time with a spatial frequency of 0.42 rad/mm. Since DMD has been applied in space, the distribution of the modes shows when certain structures occur at given frequencies. The top plot (real part of the mode) depicts a sign variation of the DMD mode in time, which identifies vortical structures within the flow field. The bottom plot (imaginary part of the mode) shows the same fluctuations shifted in time of about one-quarter of the wavelength, corresponding to the distance between the colored stripes, and describes the convective behavior of the mode.

The combined analysis of different temporal sequences and DMD modes allows pointing out the following: 1) the eigenvalues of $\tilde{S}_k^{\circ}$ provide the temporal interval with the maximum growth rate of disturbances and 2) the DMD mode distribution identifies the temporal behavior within the considered interval. As a consequence, it is possible to extract the sequences of instantaneous flow fields, where disturbances are growing and are showing a periodical behavior of the wall-normal velocity fluctuations. The instantaneous velocity fields chosen with these criteria are reported in Fig. 9 for the same case considered in Fig. 8. In more detail, the plots show the Reynolds decomposition maps of a velocity field subject to equally time-spaced perturbations. The temporal resolution is one-third of the original one. The first instant of the instantaneous velocity field corresponds to the first time instant t_0 of the DMD mode considered in Fig. 8. In Fig. 9, the vector spacing is halved with respect to the original TR-PIV resolution to improve the readability of the plot. The contour plots of the difference between the wall-normal velocity v and

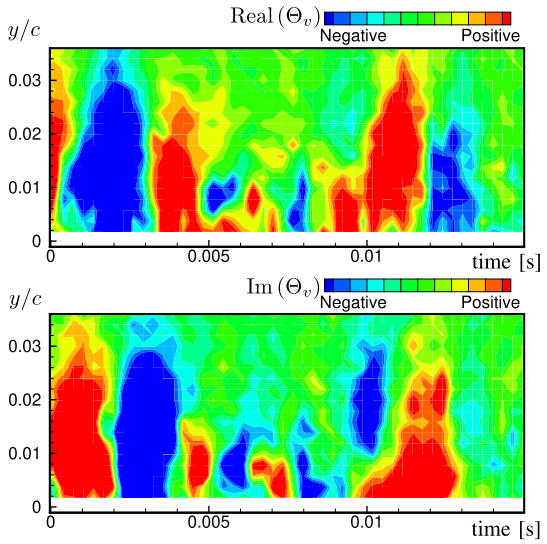

Fig. 8. Wall-normal velocity component of the DMD mode with frequency 0.42 rad/mm, Re = 75 000, and FSTI = 0.65%: contour of the real part (top) and imaginary part (bottom).

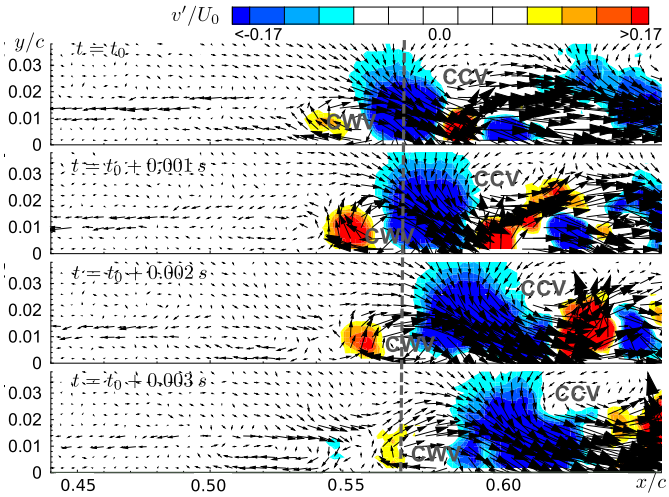

Fig. 9. Sequence of instantaneous perturbation velocity vectors (Reynolds decomposition) with Re = 75 000 and FSTI = 0.65%.

its mean (denoted by v') are also superposed to emphasize the link between the DMD mode and the flow physics. The dotted vertical gray line shows the switching point identified by the proposed approach.

Fig. 9 illustrates the formation of vortical structures. In the first instant, a small clockwise rotating vortex (marked over the plot as CWV) that induces a negative v' is generated close to the wall, just upstream of the dotted gray line. This vortex is crossing the dotted gray line in the second time snapshot at $t = t_0 + 0.001$ s. At the same time, Fig. 8 shows a negative value of the real part of Θ_v. The CWV vortex is further convected downstream: in the last plot at $t = t_0 + 0.003$ s, a positive v' is crossing the dotted gray line, and similarly, the real part of Θ_v at that time is positive. This confirms that the DMD mode contour plot reported in Fig. 8 is a marker of the vortical structures depicted here. Similarly, large counterclockwise vortices (marked as CCV) may be observed in the upper portion of the measurement domain. Such vortices are convected and grow within the identified boundaries.

V. Conclusions

We have presented a novel approach to detect changes of the regime in fluid flows by using the DMD and MHE approaches with a switching trend model. The combination of such techniques turns out to be effective, as shown through the application to experimental data sets for different values of Re and FSTI.

The successful results suggest various directions of improvement. For example, a future goal is the development of more complex switching models that are able to identify more regimes by exploiting additional information on the underlying flow physics. The use of fast MHE techniques will be addressed as well to perform optimization within a time constraint that allows applying a stabilizing feedback to the fluid flow.

References

[1] T. A. Zaki, "From streaks to spots and on to turbulence: Exploring the dynamics of boundary layer transition," *Flow, Turbulence Combustion*, vol. 91, no. 3, pp. 451–473, 2013.

[2] L. Brandt, F. Schlatter, and D. S. Henningson, "Transition in boundary layers subject to free-stream turbulence," *J. Fluid Mech.*, vol. 517, pp. 167–198, Sep. 2004.

[3] V. N. Rao, R. Jefferson-Loveday, P. G. Tucker, and S. Lardeau, "Large eddy simulations in turbines: Influence of roughness and free-stream turbulence," *Flow, Turbulence Combustion*, vol. 92, nos. 1–2, pp. 543–561, 2014.

[4] A. Mandal, L. Venkatakrishnan, and J. Dey, "A study on boundary-layer transition induced by free-stream turbulence," *J. Fluid Mech.*, vol. 660, pp. 114–146, Oct. 2010.

[5] D. Lengani, D. Simoni, M. Ubaldi, P. Zunino, and F. Bertini, "Experimental study of free-stream turbulence induced transition in an adverse pressure gradient," *Exp. Therm. Fluid Sci.*, vol. 84, pp. 18–27, Jun. 2017.

[6] D. Lengani, D. Simoni, M. Ubaldi, P. Zunino, and F. Bertini, "Experimental investigation on the time–space evolution of a laminar separation bubble by proper orthogonal decomposition and dynamic mode decomposition," *J. Turbomach.*, vol. 139, no. 3, pp. 1–8, 2017, Art. no. 031006.

[7] C. W. Rowley, T. Colonius, and R. M. Murray, "Model reduction for compressible flows using POD and Galerkin projection," *Phys. D, Nonlinear Phenomena*, vol. 189, nos. 1–2, pp. 115–129, Feb. 2004.

[8] D. Lengani, D. Simoni, M. Ubaldi, P. Zunino, and F. Bertini, "Analysis of the Reynolds stress component production in a laminar separation bubble," *Int. J. Heat Fluid Flow*, vol. 64, pp. 112–119, Apr. 2017.

[9] D. Lengani, D. Simoni, R. Pichler, R. Sandberg, V. Michelassi, and F. Bertini, "Identification and quantification of losses in a LPT cascade by POD applied to LES data," *Int. J. Heat Fluid Flow*, vol. 70, pp. 28–40, Apr. 2018.

[10] P. J. Schmid, "Dynamic mode decomposition of numerical and experimental data," *J. Fluid Mech.*, vol. 656, pp. 5–28, Jan. 2010.

[11] S. S. Chughtai and H. Werner, "Modeling and distributed control of transition in plane Poiseuille flow," *IEEE Trans. Control Syst. Technol.*, vol. 20, no. 3, pp. 755–762, May 2012.

[12] M. Milovanovic and O. M. Aamo, "Attenuation of vortex shedding by model-based output feedback control," *IEEE Trans. Control Syst. Technol.*, vol. 21, no. 3, pp. 617–625, May 2013.

[13] A. Wynn, D. Pearson, B. Ganapathisubramani, and P. Goulart, "Optimal mode decomposition for unsteady flows," *J. Fluid Mech.*, vol. 733, pp. 473–503, Oct. 2013.

[14] K. K. Chen, J. H. Tu, and C. W. Rowley, "Variants of dynamic mode decomposition: Boundary condition, Koopman, and Fourier analyses," *J. Nonlinear Sci.*, vol. 22, no. 6, pp. 887–915, Mar. 2012.

[15] M. S. Hemati, C. W. Rowley, E. A. Deem, and L. N. Cattafesta, "De-biasing the dynamic mode decomposition for applied Koopman spectral analysis of noisy datasets," *Theor. Comput. Fluid Dyn.*, vol. 31, no. 4, pp. 349–368, 2017.

[16] M. R. Jovanović, P. J. Schmid, and J. W. Nichols, "Sparsity-promoting dynamic mode decomposition," *Phys. Fluids*, vol. 26, no. 2, 2014, Art. no. 024103.

[17] R. Goebel, R. Sanfelice, and A. Teel, *Hybrid Dynamical Systems: Modeling, Stability, and Robustness*. Princeton, NJ, USA: Princeton Univ. Press, 2012.

[18] P. G. Otanez and M. E. Campbell, "Bounded switched linear estimator for smooth nonlinear systems," *IEEE Trans. Control Syst. Technol.*, vol. 15, no. 2, pp. 358–368, Mar. 2007.

[19] Y. Li, L. Ding, and G. Liu, "Error-tolerant switched robust extended Kalman filter with application to parameter estimation of wheel-soil interaction," *IEEE Trans. Control Syst. Technol.*, vol. 22, no. 4, pp. 1448–1460, Jul. 2014.

[20] J. M. Pak, C. K. Ahn, Y. S. Shmaliy, P. Shi, and M. T. Lim, "Switching extensible FIR filter bank for adaptive horizon state estimation with application," *IEEE Trans. Control Syst. Technol.*, vol. 24, no. 3, pp. 1052–1058, May 2016.

[21] Y. Li, Y. Tan, R. Dong, and H. Li, "State estimation of macromotion positioning tables based on switching Kalman filter," *IEEE Trans. Control Syst. Technol.*, vol. 25, no. 3, pp. 1076–1083, May 2017.

[22] A. Alessandri, P. Bagnerini, M. Gaggero, D. Lengani, and D. Simoni, "Dynamic mode decomposition for the inspection of three-regime separated transitional boundary layers using a least squares method," *Phys. Fluids*, vol. 31, no. 4, 2019, Art. no. 044103.

[23] A. Alessandri, P. Bagnerini, M. Gaggero, D. Lengani, and D. Simoni, "Moving horizon trend identification based on switching models for data driven decomposition of fluid flows," in *Proc. IEEE Conf. Decis. Control (CDC)*, Miami Beach, FL, USA, Dec. 2018, pp. 2138–2143.

[24] O. Marxen, M. Lang, and U. Rist, "Vortex formation and vortex breakup in a laminar separation bubble," *J. Fluid Mech.*, vol. 728, pp. 58–90, Aug. 2013.

[25] D. Simoni, D. Lengani, M. Ubaldi, P. Zunino, and M. Dellacasagrande, "Inspection of the dynamic properties of laminar separation bubbles: Free-stream turbulence intensity effects for different Reynolds numbers," *Exp. Fluids*, vol. 58, p. 66, Jun. 2017.

[26] T. Michelis, S. Yarusevych, and M. Kotsonis, "On the origin of spanwise vortex deformations in laminar separation bubbles," *J. Fluid Mech.*, vol. 841, pp. 81–108, Apr. 2018.

[27] S. Hosseinverdi and H. F. Fasel, "Numerical investigation of laminar–turbulent transition in laminar separation bubbles: The effect of free-stream turbulence," *J. Fluid Mech.*, vol. 858, pp. 714–759, Jan. 2019.

[28] A. Alessandri, M. Baglietto, and G. Battistelli, "Receding-horizon estimation for switching discrete-time linear systems," *IEEE Trans. Autom. Control*, vol. 50, no. 11, pp. 1736–1748, Nov. 2005.

[29] A. Alessandri, M. Baglietto, and G. Battistelli, "A maximum-likelihood Kalman filter for switching discrete-time linear systems," *Automatica*, vol. 46, no. 11, pp. 1870–1876, 2010.

[30] Y. Wan, T. Keviczky, M. Verhaegen, and F. Gustafsson, "Data-driven robust receding horizon fault estimation," *Automatica*, vol. 71, pp. 210–221, Sep. 2016.

[31] A. Alessandri and M. Awawdeh, "Moving-horizon estimation with guaranteed robustness for discrete-time linear systems and measurements subject to outliers," *Automatica*, vol. 67, pp. 85–93, May 2016.

[32] A. Alessandri, M. Baglietto, G. Battistelli, and M. Gaggero, "Moving-horizon state estimation for nonlinear systems using neural networks," *IEEE Trans. Neural Netw.*, vol. 22, no. 5, pp. 768–780, May 2011.

[33] A. Alessandri and M. Gaggero, "Fast moving horizon state estimation for discrete-time systems using single and multi iteration descent methods," *IEEE Trans. Autom. Control*, vol. 62, no. 9, pp. 4499–4511, Sep. 2017.

[34] Y. Guo and B. Huang, "Moving horizon estimation for switching nonlinear systems," *Automatica*, vol. 49, no. 11, pp. 3270–3281, Nov. 2013.

[35] A. Alessandri, M. Baglietto, and G. Battistelli, "Moving-horizon state estimation for nonlinear discrete-time systems: New stability results and approximation schemes," *Automatica*, vol. 44, no. 7, pp. 1753–1765, Jul. 2008.

[36] A. Alessandri, M. Baglietto, and G. Battistelli, "Luenberger observers for switching discrete-time linear systems," *Int. J. Control*, vol. 80, no. 12, pp. 1931–1943, 2007.

[37] S. Hanba, "Further results on the uniform observability of discrete-time nonlinear systems," *IEEE Trans. Autom. Control*, vol. 55, no. 4, pp. 1034–1038, Apr. 2010.

[38] D. Simoni, D. Lengani, and R. Guida, "A wavelet-based intermittency detection technique from PIV investigations in transitional boundary layers," *Exp. Fluids*, vol. 57, p. 145, Sep. 2016.